Journal of Materials Science: Materials in Electronics
https://doi.org/10.1007/s10854-020-03801-0

The effect of radiation on the forward and reverse bias current–voltage (*I–V*) characteristics of Au/($Bi_4Ti_3O_{12}$/SiO_2)/*n*-Si (MFIS) structures

S. Dulkadir[1] · H. Uslu Tecimer[2] · F. Parlaktürk[3] · Ş. Altındal[4] · Ö. Karal[5]

Received: 25 April 2020 / Accepted: 13 June 2020

Abstract
Determining the radiation effects on the basic electrical parameters of the fabricated high-dielectric MFIS structures, they were exposed to the high-energy ^{60}Co γ-rays. For this purpose, the values of ideality factor (n), barrier height (Φ_B) and series resistance (R_s) were extracted from the forward bias *I–V* data before and after irradiation by using various methods such as standard thermionic emission (TE) theory, Cheung's and Norde functions. Additionally, the energy-dependent profile of surface states N_{ss} was extracted by considering voltage dependence of n, Φ_B and R_s and compared each other. Experimental results show that the reverse saturation current (I_o), n and R_s values increase with increasing radiation dose, but Φ_B decreases. When the value of R_s is considered in the calculation of N_{ss}, they were found to be considerably decreased. The observed low discrepancies between N_{ss} after irradiation show that the use of a high-dielectric ferroelectric interlayer leads to an increase in the resistance of MS to radiation. It is more important to fabricate radiation-resisted electronic device, especially in the satellites due to hard radiation in space. As a result, N_{ss}, R_s and the existence of interlayer are more effectual on the *I–V* characteristics which must be considered in the electrical parameter calculation.

1 Introduction

The bismuth titanite ($Bi_4Ti_3O_{12}$) is a high-dielectric ferroelectric materials such as barium oxide ($BaTiO_3$) and strontium oxide ($SrTiO_3$) and it has high-charge storage capacity/energy, wide bandgap (E_g), high breakdown strength, low coercive field, high Curie temperature (675 °C) and peculiar switching behavior [1–5]. Therefore, $Bi_4Ti_3O_{12}$ (BTO), which is belonging to Aurivillius family, has attracted significant interest in the applications of devices such as optical and electro-optic devices, ferroelectric field-effect transistors (FeFETs), nonvolatile ferroelectric random-access memories (FeRAMs) and memory storage capacitors (MSCs) [6–8]. Among bismuth-layer-structure ferroelectrics, $Bi_4Ti_3O_{12}$ films are the simplest, environment friendly and prominent compound. They are particularly attractive due to the high-speed transistor-based nonvolatile memories and nature of high densities [4–8]. FeRAMs have a wide operating temperature range, superior speed performance, high information density, the ability to serve in harsh environments and limitless write-to-read cycles [9, 10]. In addition, a metal-ferroelectric-metal (MFM)-type capacitor has been studied for many years to form FeRAMs.

In order to avoid interface diffusion between the semiconductor and ferroelectric layer, a thin insulator layer like Si_3N_4, SnO_2 and also SiO_2 is inserted at the BTO/Si interlayer [11, 12]. In the light of the above-mentioned information, MFS type is evolved into a metal-ferroelectric-insulator-semiconductor (MFIS)-type structure. Thanks to this thin layer, the electric field reducing problem in the MFIS structure is decreased, while the reaction and interdiffusion between the ferroelectric layer and the semiconductor is prevented. The SiO_2 is a stable and promising structure,

✉ H. Uslu Tecimer
habibeuslu@karabuk.edu.tr

1 Electric and Electronic Engineering Department, Engineering Faculty, Karabuk University, Karabuk, Turkey

2 Medical Engineering Department, Engineering Faculty, Karabuk University, Karabuk, Turkey

3 Turkish Atomic Energy Agency, Lodumlu, 06690 Ankara, Turkey

4 Department of Physics, Gazi University, 06500 Ankara, Turkey

5 Electric and Electronic Engineering Department, Natural Sciences and Engineering Faculty, Ankara Yıldırım Beyazıt University, Ankara, Turkey

Published online: 22 June 2020

especially with the ability to regulate load transitions, prevent internal diffusion and reduction in electric field, and precisely control the gate potential from the FET channel. Thanks to these features, in this study, SiO_2 was preferred as an insulator layer in MFIS structures. However, the magnitude of the applied bias reduction caused by interlayer depends on the capacitance ratio of the BTO film and the interlayer.

In an MFIS structure, the metal and semiconductor are separated by an interlayer and the distribution of N_{ss} at the semiconductor/interlayer interface is continuous. For the electrical behavior of a metal–insulator/ferroelectric-semiconductor (MIS/MFS) and MFIS structures, R_s and N_{ss} are important parameters affecting these structures [13–31]. Although the main parameters of these structures have been studied under different conditions extensively, the irradiation effect on them has not been identified yet. For this reason, the identification of the irradiation effect on main electrical parameters at various irradiation doses is the goal of this study. Even though many methods have been developed for the determination of the after-irradiation behavior of interband radiation-induced of N_{ss} at the MIS type, Ma [32, 33], Winokur et al. [34], Da Silva et al. [35] and Tataroğlu et al. [36, 37] were among the pioneers who made systematic observations. Permanent and temporary effects of irradiation, which cause changes in crystal lattices, occur due to bombardment of the devices by irradiation and the generation of an electron–hole pair, respectively [38]. The radiation-generated holes which are less mobile than the electrons may diffuse in the interlayer, and also many stationary hole traps are existing.

In our previous studies [2, 8, 16, 18, 30, 31], both electrical and dielectric properties of the fabricated Al/p-Si and Au/*n*-Si (MS) SBDs with a thin high-dielectric $Bi_4Ti_3O_{12}$ (BTO) interfacial layer have been investigated as function of frequency, temperature and voltage in detail. All these results have confirmed that the use of such high-dielectric interlayer leads to an increase in the performance of MS-type SBDs in respect of low series resistance (R_s), low surface states (N_{ss}), low leakage current, high capacitance, and hence can have more storage electrons or energy like an ultra-capacitor. Similarly, Yıldırım et al. for Au/$Bi_3Ti_4O_{12}$/*n*-Si [14] and Reddy et al. [5] for Au/$BaTiO_3$/n-GaN MIS-type structures show that MIS-type structure has a higher rectification rate with low reverse saturation current and surface states. Additionally, Çetinkaya et al. [2, 18] show that both the electrical and dielectric of these SBDs may be changed from one diode to another even at identically fabricated of them. Therefore, radiation dependence of electrical characteristics has been investigated in this study by using forward and reverse bias *I–V* measurements before and after gamma radiation. Radiation-dependent capacitance–voltage (*C–V*) and conductance–voltage (G/ω–V) characteristics of these SBDs are also under our investigation and will be published soon, as the second part of this study.

The main purpose of this study is to achieve a better understanding of irradiation effect on main electrical parameters (I_o, n, Φ_B, R_s) by measuring the forward bias *I–V* measurements. Detailed analysis of the Au/($Bi_4Ti_3O_{12}$/SiO_2)/*n*-Si structure, exposed to the maximum cumulative dose of 22 kGy at room temperature, was reported. Also, the $N_{ss} - (E_c - E_{ss})$ profile of structure were extracted by considering voltage dependence of n, Φ_B and R_s and comparing each other. Experimental data indicate that the basic electrical parameters are extremely dependent on radiation dose.

2 Experimental procedures

Au/($Bi_4Ti_3O_{12}$/SiO_2)/*n*-Si structures were performed on the phosphor-doped (*n*-Si) wafer with (100) direction, 0.7 Ω cm resistivity, 300 μm thickness and 5.08 cm diameter. In the first stage, organic solvents ($CHClCCl_2$, CH_3COCH and CH_3OH) were used for degreasing of *n*-Si wafer. Later, *n*-Si wafer was etched in a sequence of H_2SO_4, H_2O_2, 20% HF, a solution of $6HNO_3$:1HF:$35H_2O$, 20% HF. During surface cleaning of *n*-Si wafer, at each step, the wafer was rinsed in ultrapure deionized water (DW) having resistivity of 18 MΩ cm at about 10 min. In the second stage, *n*-Si wafer was transferred into high-vacuum thermal evaporation system. Here, it was deposited with 99.999% purity Au layer at 1 μTorr and then annealed at 550 °C in nitrogen ambient with a flow rate of 2 l/min at for 20 min to get good ohmic contact. Thirdly, *n*-Si wafer was taken into RF magnetron sputtering device where it was deposited with $Bi_4Ti_3O_{12}$ (BTO) ferroelectric film by using a hot compacting of BTO powder of a stoichiometric composition as a target material.

A Veeco Dektak 6 M thickness profilometer was utilized for measuring thickness of interfacial BTO layer as 2.4 nm [16, 30, 31]. Ar and O_2 gases' mixture was used as a working medium and the structure was kept at 700 °C for settling. The thin layer of SiO_2 at the BTO/Si interface was assumed to grow during annealing of the BTO films in air ambient. Finally, the ($Bi_4Ti_3O_{12}$/SiO_2/*n*-Si/Au) sample was immediately transferred into thermal evaporation system and then Au rectifier contacts were thermally evaporated onto $Bi_4Ti_3O_{12}$ film with the help of a mask with 1 mm diameter. Thus, the formation of the MFIS structure was completed and its schematic diagram is given in Fig. 1. The *I–V* measurements of the MFIS structures were completed by using Keithley 2400 *I–V* source meter. The measurements were carried out before and after ^{60}Co (γ-ray) source irradiation with the dose of 2.12 kGy/h and total dose range was 0–22 kGy.

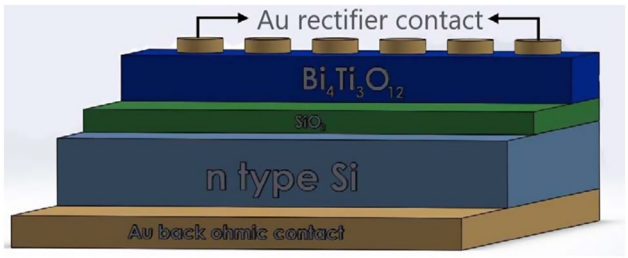

Fig. 1 The schematic presentation of the structure

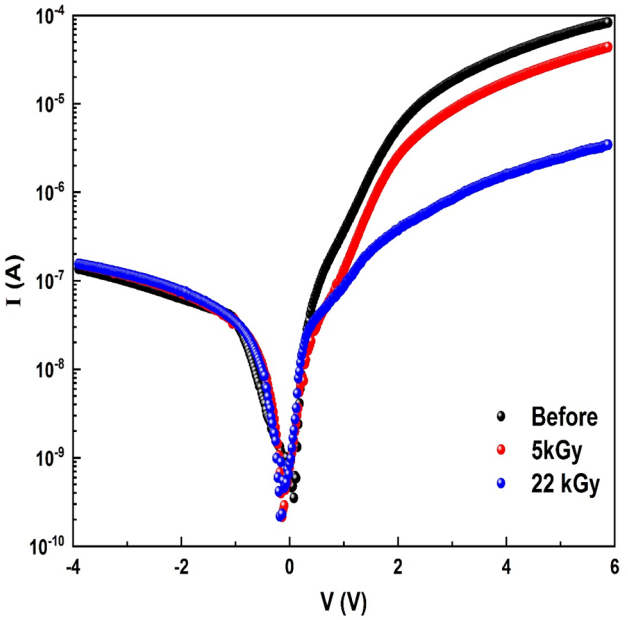

Fig. 2 *I–V* graphs of the structure

3 Results and discussion

It is generally known that radiation has two important effects on materials that we can classify permanently and temporarily [39]. If deterioration occurs due to radiation effects in crystal lattices, which have great importance, permanent effects can be seen in the structures. Also, temporary effects may occur due to the generation of an electron–hole pair. To understand these effects in detail, the radiation impact on the *I–V* characteristics in MFIS structures has been investigated. *I–V* measurements were performed before radiation and after various radiation doses which consist of 5 kGy, 22 kGy. Forward and reverse bias *I–V* data of the structure, before and after γ-ray irradiation from ^{60}Co gamma source, and measurements of which were carried out between −4/+6 V, are presented in Fig. 2. *I* vs *V* plots of Au/$Bi_4Ti_3O_{12}$/SiO_2/*n*-Si (MFIS) structures have two distinct linear regions with different slopes as clearly seen from Fig. 2. The first linear region is expressed as Region I in the 0.12–0.38 V voltage range and the second linear region is expressed as Region II in the 0.40–0.80 V. Double parallel diode model can be utilized to explain such multi-linear regions. As tabulated in Table 1, related with irradiation, three main parameters (Φ_{Bo}, I_o and n) of the structure for both Region I and Region II were acquired. Although the increase of the radiation dose to 22 kGy decreased the forward current value, it had no effect on the reverse bias current.

The correlation between current and applied forward biases can be written due to the thermionic emission (TE) as [40]

$$I = I_{o1}\left\{\exp\left(\frac{q(V-IR_s)}{n_1kT}\right)-1\right\} + I_{o2}\left\{\exp\left(\frac{q(V-IR_s))}{n_2kT}\right)-1\right\}+\frac{V-IR_s}{R_{sh}}. \quad (1)$$

In the formula, reverse saturation currents, Region I and Region II ideality factors and series and shunt resistors are shown with I_{o1} and I_{o2}, n_1 and n_2 and R_s and R_{sh}, respectively. Besides, IR_s corresponds to the voltage drop on the R_s. Moreover, the components of diffusion and recombination generation currents were depicted by the first and second terms in Eq. 1, respectively. In Eq. 1, the terms of I_{o1} and I_{o2} are can be extracted from the straight-lines intercept of ln(*I*)–*V* plots at zero bias and can be expressed as:

$$I_{o1} = AA^*T^2\exp\left(-\frac{q\Phi_{Bo1}}{kT}\right) \quad I_{o2} = AA^*T^2\exp\left(-\frac{q\Phi_{Bo2}}{kT}\right), \quad (2)$$

where the quantities A^* and A are the effective Richardson constant (120 A/cm^2 K^2 for n-type Si) and the rectifier contact area (7.85×10^{-3} cm^2), respectively. Two linear regions

Table 1 The basic electrical parameters of the structure

	Region I			Region II			Ohm's law	
	I_{o1} (A)	n_1	Φ_{Bo1} (eV)	I_{o2} (A)	n_2	Φ_{Bo2} (eV)	R_{sh} (Ω)	R_s (Ω)
Before	2.15×10^{-10}	2.63	0.839	1.21×10^{-8}	10.89	0.738	2.82×10^{7}	7.20×10^{4}
5 kGy	1.14×10^{-9}	5.04	0.797	7.75×10^{-9}	14.25	0.749	2.50×10^{7}	1.30×10^{5}
22 kGy	2.25×10^{-9}	5.32	0.780	1.65×10^{-8}	23.73	0.730	2.51×10^{7}	1.66×10^{6}

slope at forward biases were utilized to determine the n values of MFIS structures as follows:

$$n_1 = \frac{q}{kT\tan\theta_1} \quad n_2 = \frac{q}{kT\tan\theta_2}. \tag{3}$$

Thus, the value of Φ_{Bo} can be obtained from Eq. 4 by using A and I_o,

$$\Phi_{Bo1} = \frac{kT}{q}\ln\left(\frac{AA^*T^2}{I_{o1}}\right) \quad \Phi_{Bo2} = \frac{kT}{q}\ln\left(\frac{AA^*T^2}{I_{o2}}\right). \tag{4}$$

In order to analyze radiation effects in more detail, it is of great importance to calculate some basic parameters such as n and Φ_{Bo}. Thus, the basic diode parameters calculated in the light of the equations given above are shown in Table 1.

As clearly seen from Table 1, I_o values increase after exposure of the structure to the with increasing radiation dose. I_o values for Region I changed from 2.15×10^{-10} to 2.25×10^{-9} and Region II 1.21×10^{-8} A to 1.65×10^{-8} A. This radiation-induced change observed in I_o value could be attributed to the interfacial defect density increment [39]. There is an inverse proportion between the barrier height and reverse saturation current.

Depending on increasing irradiation dose, a decrease in Φ_{Bo} was observed. According to some previous studies, γ-irradiation affects the free carrier concentration as it induces imperfections in the bandgap at the junction of the semiconductor [41, 42]. That is why radiation is an important factor for the barrier height in the structures and the barrier height value in Region I is close to the barrier height value in Region II and the value in Region I is higher than the value in Region II. According to recent studies in this field, X-ray photoelectron spectroscopy analysis points out defect generation which reduced the barrier height and enhanced tunneling effects, in Si dangling bonds [43].

While the values of ideality factor n in the first region were found to range from 2.63 at 0 kGy (before irradiation) to 5.32 at 22 kGy (after irradiation), values of ideality factor n in the first region were found to range from 10.89 at 0 kGy to 23.73 at 22 kGy. Obviously, the n values depend on the applied biases as Region I values are much lower than Region II values. The barrier homogeneity and high N_{ss} density localized at the interlayer effects are seen as the cause of high values in Region II [1, 11, 14]. Other possible mechanisms that can lead to n values greater than unity can be listed as image force effect, recombination production and tunneling [41, 42]. The ideality factor, which increases in parallel with the increase in applied radiation doses, is evidence of the deviation from the standard TE theory.

With the dose of radiation, defect and noise ratios occur that affect the performance of the structures. One of the important factors affecting this performance is resistance values. Utilizing from Ohm's law ($R_i = V_i/I_i$), the resistance (R_i) of the Au/$Bi_4Ti_3O_{12}$/SiO_2/n-Si (MFIS) structure was calculated between − 4 V/6 V. R_i values are extremely depending on biases as presented in Fig. 3. R_i values correspond to R_{sh} and R_s for high negative biases and high positive biases, respectively.

According to Table 1, it was observed that R_{sh} values remained almost constant, while R_s values increased in parallel with the increase in irradiation doses. This increase in R_s value indicates that free carrier density and mobility are reduced [44]. The reason for the decrease in mobility is the settlement of the defect centers that serve as a reunification center together with irradiation. The free carrier density will decrease when deep traps settle inside the material in relation to the displacement of the point defects. The intensity of irradiation-induced defect (trap) centers increases. Thus, the free carriers in the crystal lattice are captured by the defect (trap) centers and, consequently, a decrease in the carrier density is observed.

Another way used to determine n, $\Phi_{B(Cheung)}$ and R_s values is a method which was carried out from the functions developed by Cheung method [45]. Cheung functions are defined using Eq. 1 as follows:

$$\frac{dV}{d\ln(I)} = n\frac{kT}{q} + R_sI, \tag{5}$$

$$H(I) = V - n\frac{kT}{q}\ln\left(\frac{I}{AA^*T^2}\right) = n\Phi_{B(Cheung)} + R_sI, \tag{6}$$

where $\Phi_{B(Cheung)}$ is the barrier height obtained from the intercept of $H(I)$ vs I plots and IR_s is the voltage drop across the series resistance of MFIS structure. The dV/dln (I) and $H(I)$–I curves obtained with the Cheung functions have linear lines and R_s values are obtained from the slope of these

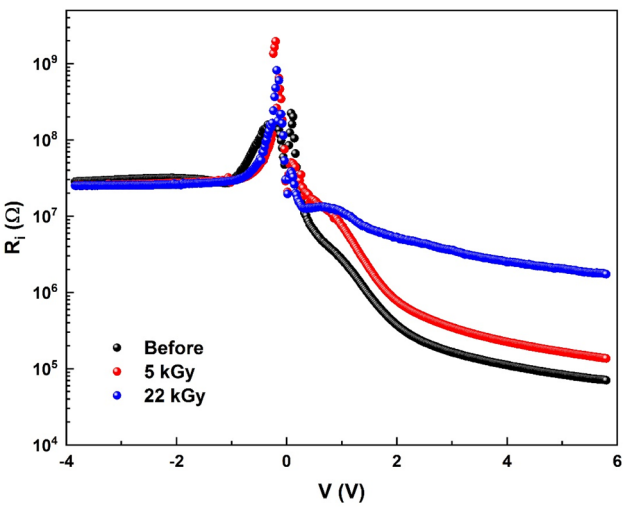

Fig. 3 R_i characteristics of the structure

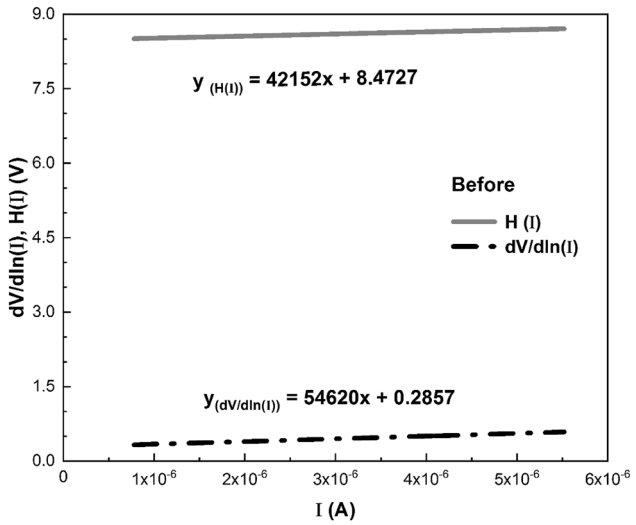

Fig. 4 d*V*/d ln (*I*)/*H*(*I*)–*I* plots of the structure for before radiation

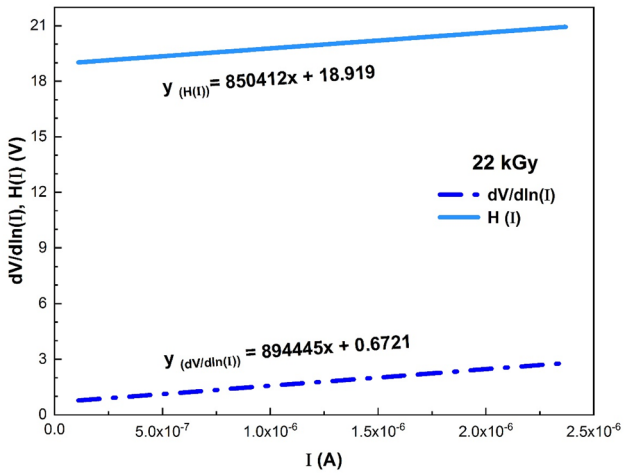

Fig. 6 d*V*/d ln (*I*)/*H*(*I*)–*I* plots of the structure for 22 kGy

lines before and after the irradiation of the structure. Cheung functions curves for MFIS structure are given in Fig. 4 for before radiation, Fig. 5 for 5 kGy and Fig. 6. for 22 kGy. All figures indicate that Cheung functions curves are linear lines. R_s, n and $\Phi_{B(Cheung)}$ values curves are given in Table 2. As can be seen in Table 2, the obtained R_s values by Cheung functions are compatible with each other and increase with the increasing irradiation. The values of $\Phi_{B(Cheung)}$ were found to decrease, while the values of n increase with the increasing radiation dose ($\Phi_{B(Cheung)} = 0.740$ eV and $n = 11.44$ at 0 kGy and $\Phi_{B(Cheung)} = 0.705$ eV and $n = 26.80$ at 22 kGy).

On the other hand, as an alternative to the Cheung functions, another method can be also used presented by Norde to calculate some basic parameters [46]. Unlike Cheung

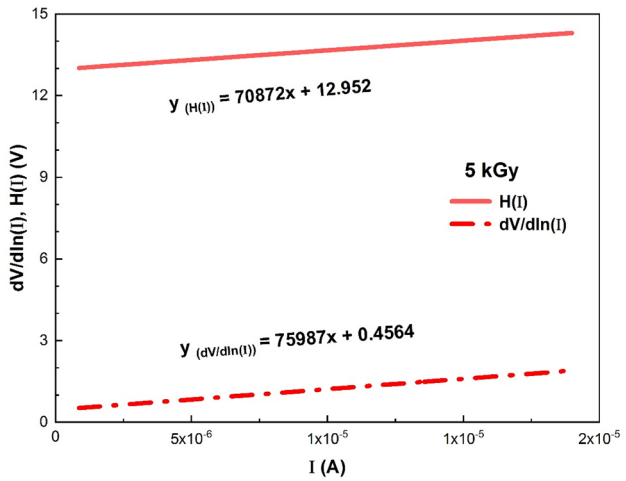

Fig. 5 d*V*/d ln (*I*)/*H*(*I*)–*I* plots of the structure for 5 kGy

functions, Norde function not only applied to the nonlinear region for the higher forward biases, but also applied to the full forward biases at *I*–*V* curve [47]. The modified Norde method is given as follows:

$$F(V) = \frac{V}{\gamma} - \frac{kT}{q}\ln\left(\frac{I}{AA^{*}T^{2}}\right), \tag{7}$$

where γ is the dimensionless value greater than the ideality factor which is extracted from the ln(*I*)–*V* plots. γ values are 16.34 at before radiation, 19.96 at 5 kGy and 30.85 at 22 kGy. Using the minimum point of $F(V)$ vs V plot, $F(V_o)$, $\Phi_{B(Norde)}$ and R_s can be obtained from the following equations, respectively.

$$\Phi_{B(Norde)} = F(V_o) + \frac{V_o}{\gamma} - \frac{kT}{q} \tag{8a}$$

$$R_s = \frac{(\gamma - n)kT}{qI_m}. \tag{8b}$$

Figure 7 shows the F(V) vs V plots for the Au/$Bi_4Ti_3O_{12}$/SiO_2/*n*-Si (MFIS) structures. The values of $\Phi_{B(Norde)}$ and R_s acquired from Eqs. (8a) and (8b) under various irradiation conditions are presented in Table 2. The values of R_s calculated from Norde and Cheung methods are different from each other. As clearly seen in Table 2, the barrier height and series resistance values obtained from Norde theory are higher than those extracted from Cheung's functions. These variations in values acquired by using different methods may be result from the extraction in change regions of the *I*–*V* curves. Furthermore, as we mentioned above, there are differences in the basic parameters as the areas of application of the Norde and Cheung are different from each other.

Considering the voltage-dependent $n(V)$ and effective barrier height (Φ_e), N_{ss} in equilibrium with the semiconductor

Table 2 Basic electrical parameters of the structure obtained from Cheung and Norde functions

	d*V*/d ln (I) – *I*		*H*(*I*)–*I*		Norde (Region I)		Norde (Region II)	
	R_s (Ω)	*n*	R_s (Ω)	$\Phi_{B(Cheung)}$ (eV)	R_s (Ω)	$\Phi_{B(Norde)}$ (eV)	R_s (Ω)	$\Phi_{B(Norde)}$ (eV)
Before	5.46×10^4	11.44	4.22×10^4	0.740	9.99×10^5	0.757	4.65×10^4	0.813
5 kGy	7.60×10^4	18.00	7.09×10^4	0.722	2.80×10^6	0.771	7.03×10^4	0.803
22 kGy	8.94×10^5	26.80	8.50×10^5	0.705	5.26×10^6	0.739	5.26×10^5	0.765

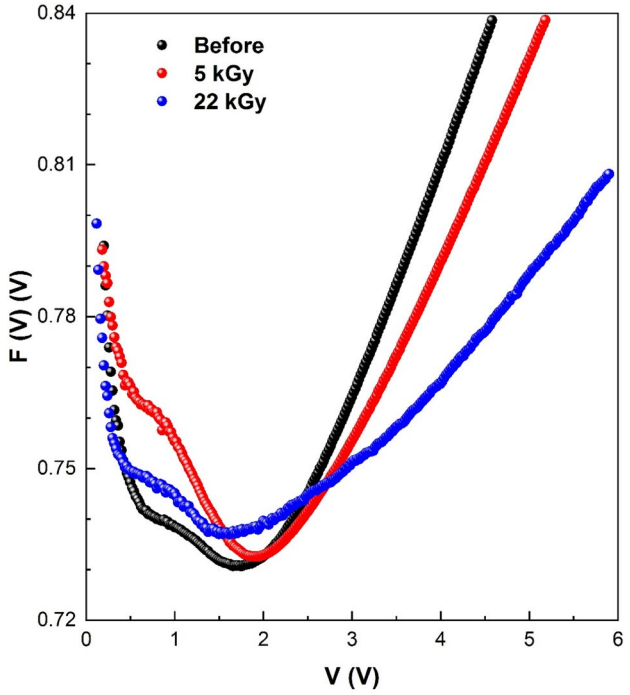

Fig. 7 *F*(*V*)–*V* plots of the structure

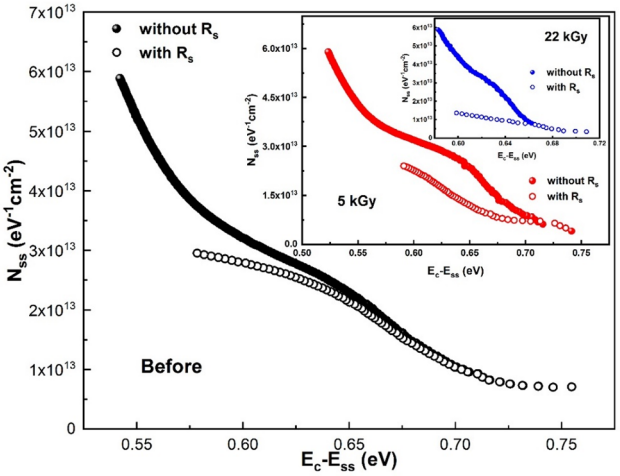

Fig. 8 The density of *N*ss profiles as a function of ($E_c - E_{ss}$)

can be specified from the forward bias *I*–*V* data [48]. Regardless of R_s values, the values of Φ_e and $n(V)$ can be calculated using Eqs. (9) and (10). Φ_e is presumed to be voltage-dependent and derived by the following expression:

$$\Phi_e = \Phi_{Bo} + \beta(V - IR_s) = \Phi_{Bo} + \left(1 - \frac{1}{n(V)}\right)(V - IR_s). \tag{9}$$

Here the voltage coefficient of the Φ_e is denoted by β. For MFIS structure, having the N_{ss} in equilibrium with semiconductor and voltage-dependent ideality factor is expressed as

$$n(V) = \frac{q}{kT}\left[\frac{(V - IR_s)}{\ln\left(I/I_o\right)}\right] = 1 + \frac{\delta}{\varepsilon_i}\left[\frac{\varepsilon_s}{W_D} + qN_{ss}(V)\right], \tag{10}$$

where the depletion layer width is denoted by W_D and the interlayer and semiconductor permittivities are denoted by ε_i and ε_s, respectively. This expression of $n(V)$ is identical to Eq. 11 of Card and Rhoderick [49] and the expression for N_{ss} is converted to

$$N_{ss}(V) = \frac{1}{q}\left[\frac{\varepsilon_i}{\delta}(n(V) - 1) - \frac{\varepsilon_s}{W_D}\right], \tag{11}$$

where δ the interlayer thickness (SiO_2) was obtained from the *C*–*V* measured at 1 MHz in the strong accumulation region by using the $C_{ox} = \varepsilon_i\varepsilon_o A/\delta$ and found to be 41 Å in the previous study [16, 30, 31]. Then again, the interface states' energy, E_{ss}, to the conduction band's bottom, E_c, at the semiconductor's surface is derived by [50]

$$E_c - E_{ss} = q(\Phi_e - V). \tag{12}$$

The energy distribution profile of N_{ss} as a function of ($E_c - E_{ss}$) was obtained from the forward bias *I*–*V* characteristics by taking the bias dependence of the Φ_e into account for each radiation dose. As seen in Fig. 8, the exponential growth of the N_{ss} from the with the semiconductor mid-gap toward the bottom of the conduction band is very apparent. The N_{ss} values extracted without considering the R_s are higher than those obtained taking into account the R_s. In addition, these decreases of interface states with increasing irradiation doses were attributed to the recombination of electron–hole pairs under the radiation and the existence

of an interlayer (SiO_2) at MFIS interface. Hence, R_s must be considered in calculations of basic electrical parameters.

4 Conclusions

The forward and reverse bias *I–V* characteristics of Au/$Bi_4Ti_3O_{12}$/SiO_2/*n*-Si (MFIS) structures exposed to ^{60}Co γ-irradiation of doses ranging from 0 to 22 kGy have been investigated at room temperature. While the forward current was detected to decrease with radiation dose increment, the irradiation effects on the reverse bias current were almost negligible. According to the experimental results, it was observed that the main electrical parameters such as I_o, n, Φ_B, R_s and R_{sh} values were strongly dependent on the irradiation effect. Among the main parameters which are exposed to increasing cumulative γ-ray doses, while the values of the ideality factor have an apparent increase, the values of zero-bias barrier height have a decrease. Growth in n values which increase with irradiation dose results from inhomogeneity of the interlayer and the presence of a thin insulating layer. On the other hand, another important parameter, R_s, was obtained by three different methods: Ohm's law, Cheung and Norde methods. Also, results obtained from these methods showed great compatibility with each other. The density of interface states (N_{ss}) which was determined from the forward bias *I–V* characteristics by considering the bias dependence of the Φ_e and n decreases with radiation dose increment. Such a behavior of N_{ss} was attributed to the decrease in the recombination centers and because of the irradiation and reordering/restructuring of the bandgap surface states. In conclusion, the irradiation-dependent *I–V* characteristics affirmed that R_s and N_{ss} are significant parameters that considerably affect the electrical qualifications of MFIS structures.

Acknowledgements All authors would like to thank Gazi University Scientific Research Center for the supports and contributions (Project No: GU-BAP.05/2019-26).

References

1. S.K. Badge, A.V. Deshpande, Solid State Ionics **334**, 21 (2019)
2. H.G. Çetinkaya, M. Yıldırım, P. Durmus, Ş. Altındal, J. Alloys Compd. **721**, 750 (2017)
3. S. Sruthi, A. Adarsh, A. Veronica, M. Saideep, S. Dutta, J. Mater. Sci. Mater. Electron. **27**, 4062 (2016)
4. A. Büyükbaş-Ulusan, S. Altındal Yerişkin, J. Mater. Sci. Mater. Electron. **29**, 16740 (2018)
5. V. Rajagopal-Reddy, V. Manjunath, V. Jandarhanam, Y.-H. Kill, C.-J. Cho, J. Mater. Sci. Mater. Electron. **34**, 3499 (2014)
6. Z.S. Macedo, M.H. Lente, J.A. Eiras, A.C. Hernandes, J. Phys. Condens. Matter **16**, 2811 (2004)
7. S.K. Badge, A.V. Deshpande, Ceram. Int. **45**, 15307 (2019)
8. P. Durmus, M. Yıldırım, Ş. Altındal, Curr. Appl. Phys. **13**, 1630 (2013)
9. W. Gao, Y. Zhu, Y. Wang, G. Yuan, J.M. Liu, J. Mater. **6**, 1 (2020)
10. Y. Nishi, B. Magyari-Kope (eds.), *Advances in Non-volatile Memory and Storage Technology* (Woodhead Publishing, Sawston, 2019)
11. S. Oh, J. Song, I.K. Yoo, H. Hwang, IEEE Electron. Dev. Lett. **40**, 1092 (2019)
12. D.K. Sharma, R. Khosla, S.K. Sharma, AIP Conf. Proc. **1661**, 1 (2015)
13. S.O. Tan, H. Tecimer, O. Çiçek, IEEE Electron. Dev. Lett. **64**(3), 984 (2017)
14. M. Yıldırım, M. Gökçen, Bull. Mater. Sci. **37**, 257–262 (2014)
15. İ. Taşçıoğlu, S.O. Tan, Ş. Altındal, J. Mater. Sci. Mater. Electron. **30**, 11536 (2019)
16. F. Parlaktürk, Ş. Altındal, A. Tataroğlu, M. Parlak, A. Agasiev, Microelectron. Eng. **85**, 81 (2008)
17. S.O. Tan, İ. Taşcıoğlu, S. Altındal-Yerişkin, H. Tecimer, F. Yakuphanoğlu, Silicon (2020). https://doi.org/10.1007/s12633-020-00382-9
18. H.G. Çetinkaya, M. Yıldırım, P. Durmuş, Ş. Altındal, J. Alloys Compd. **721**, 750 (2017)
19. S.O. Tan, I.E.E.E. Trans, Electron. Dev. **64**, 5121 (2017)
20. A. Tataroğlu, Chin. Phys. B **22**, 068402 (2013)
21. D.E. Yıldız, D.H. Apaydın, L. Toppare, A. Cirpan, J. Appl. Polym. Sci. **134**(19), 44817 (2017)
22. D.E. Yildiz, H.H. Gullu, A. Sarilmaz, F. Ozel, A. Kocyigit, M. Yildirim, J. Mater. Sci. Mater. Electron. **31**(2), 935 (2020)
23. F. Yigiterol, H.H. Güllü, Ö. Bayraklı, D.E. Yıldız, J. Electron. Mater. **47**(5), 2979 (2018)
24. S.B.K. Aydın, D.E. Yıldız, H.K. Çavuş, R. Şahingöz, Bull Mater. Sci. **37**(7), 1563 (2014)
25. A. Sarilmaz, F. Ozel, A. Karabulut, İ. Orak, M.A. Şahinkaya, Phys. B **580**, 411821 (2020)
26. O. Sevgili, F. Lafzi, A. Karabulut, İ. Orak, S. Bayındır, Composites B **172**, 226 (2019)
27. C. Aksu-Canbay, A. Tataroğlu, W.A. Farooq, A. Dere, A. Karabulut, M. Atif, A. Hanif, Mater. Sci. Semicond. Process. **107**, 104858 (2020)
28. A. Karabulut, A. Sarilmaz, F. Ozel, İ. Orak, M.A. Şahinkaya, Curr. App. Phys. **20**, 58 (2020)
29. A. Karabulut, Bull. Mater. Sci. **42**, 5 (2019)
30. Ş. Altındal, F. Parlaktürk, A. Tataroğlu, M. Parlak, S.N. Sarmasov, A.A. Agasiev, Vacuum **82**, 1246 (2008)
31. F. Parlaktürk, *Doktora Tezi* (Gazi Üniversitesi Fen Bilimleri Enstitüsü, Ankara, 2007), pp. 40–47
32. T.P. Ma, P.V. Dressendorfer, *Ionizing Radiation Effects in MOS Devices and Circuits* (Wiley, New York, 1989)
33. T.P. Ma, Semicond. Sci. Technol. **4**, 1061 (1989)
34. P.S. Winokur, P.S. Winokur, J.M. McGarrity, H.E. Boesch, I.E.E.E. Trans, Nucl. Sci. **23**, 1580 (1976)
35. E.F. Da Silva, Y. Nishioka, T.P. Ma, IEEE Trans. Nucl. Sci. **34**, 1190 (1987)
36. A. Tataroğlu, Ş. Altindal, M.M. Bülbül, Nucl. Instrum. Method Phys. Res. A **568**(2), 863 (2006)
37. A. Tataroğlu, Ş. Altindal, Nucl. Inst. Method Phys. Res. B **252**(2), 257 (2006)
38. A. Tataroğlu, Ş. Altindal, Nucl. Instrum. Methods Phys. Res. A. **580**, 1588 (2007)
39. Ö. Güllü, M. Çankaya, M. Biber, A. Türüt, J. Phys. D. Appl. Phys. **41**, 135103 (2008)
40. H.U. Tecimer, M.A. Alper, H. Tecimer, S.O. Tan, Ş. Altındal, Polym. Bull. **75**, 4257 (2018)
41. S.J. Fonash, S. Ashok, R. Singh, Appl. Phys. Lett. **39**, 423 (1981)
42. E. Grusell, S. Berg, L.P. Andersson, J. Electrochem. Soc. **127**, 1573 (1980)

43. Y. Xu, J. Bi, K. Xi, M. Liu, Appl. Phys. Express **12**, 061004 (2019)
44. A. Teffahi, D. Hamri, A. Mostefa, A. Saidane, N. Al Saqri, J.F. Felix, M. Henini, Curr. Appl. Phys. **16**, 850 (2016)
45. S.K. Cheung, N.W. Cheung, Appl. Phys. Lett. **49**, 85 (1986)
46. H. Norde, J. Appl. Phys. **50**, 5052 (1979)
47. M.E. Fırat, M.A. Taştan, Ş. Karataş, Mater. Today Proc. **18**, 1946 (2019)
48. S. Demirezen, Z. Sönmez, U. Aydemir, S. Altndal, Curr. Appl. Phys. **12**, 266 (2012)
49. H.C. Card, E.H. Rhoderick, J. Phys. D **4**, 319 (1971)
50. H. Uslu, Ş. Altindal, U. Aydemir, I. Dökme, I.M. Afandiyeva, J. Alloys Compd. **503**, 96 (2010)